Study of the Photoluminescence Enhancement Observed in ZnO Nanowire Gratings Optimally Grown by the Hydrothermal Method

Aubry Martin, Audrey Potdevin, François Réveret, Emmanuel Centeno, Rafik Smaali, Fatima Omeis, David Riassetto, Elena Kachan, Yves Jourlin, Geneviève Chadeyron, et al.

Study of the photoluminescence enhancement observed in ZnO nanowire gratings optimally grown by hydrothermal method

Aubry Martin[1,2], Audrey Potdevin[2,], François Réveret[2], Emmanuel Centeno[3], Rafik Smaali[3], Fatima Omeis[3-4], David Riassetto[1], Elena Kachan[4], Yves Jourlin[4], Geneviève Chadeyron[2] and Michel Langlet[1,£]*

[1] Université Grenoble Alpes, CNRS, Grenoble INP, LMGP, 38000 Grenoble, France

[£] e-mail : michel.langlet@lmgp.grenoble-inp.fr

[2] Université Clermont Auvergne, CNRS, Clermont Auvergne INP, ICCF, F-63000 Clermont–Ferrand, France. *e-mail: audrey.potdevin@sigma-clermont.fr

[3] Université Clermont Auvergne, CNRS, Clermont Auvergne INP, Institut Pascal, F-63000 Clermont–Ferrand, France.

[4] Laboratoire Hubert Curien, Université Jean-Monnet, Université de Lyon, IOGS, UMR CNRS 5516, 42000 Saint-Etienne, France

Keywords: ZnO nanowires, resonant gratings, photoluminescence enhancement, electromagnetic simulations

An original ZnO nanowire (NW) architecture has been developed, entirely based on a soft chemistry approach, and thoroughly assessed through optical measurements and electromagnetic simulations. This architecture relies on the photo-imprinting of a sol-gel ZnO-based photosensitive seed layer combined with the subsequent localized hydrothermal growth of ZnO NWs. The optimization of the elaboration protocol has been shown to lead to uniform and reproducible linear and periodic gratings of ZnO NWs with a width / pitch of 2 µm / 4 µm. The NW gratings are compared with full-covered samples (NWs coating) elaborated from a non-imprinted seed layer. A morphological study reveals that NW gratings present a peculiar hedgehog-like profile. Standard and angle-resolved photoluminescence study demonstrates that ZnO NWs visible emission is strongly modified by the presence of NW gratings and that its red part is directionally extracted and enhanced by a factor of up to 2. The electromagnetic simulations performed for both samples highlight the role of the gratings acting as coupled microcavities that boost the ZnO emission through light localization and diffractive mechanisms. It enables the extraction of the resonant photons at specific angles and wavelengths.

1. Introduction

Nanowires (NWs) are advanced structures developed in recent years for multiple applications, due to their high aspect ratio (length to width ratio) inducing specific properties which differ from bulk materials[1]. This is due to the fact that electrons are laterally quantum confined in the NWs and thus occupy different energy levels[2]. For example, bulk silicon presents an indirect band-gap, while silicon nanowires have a direct band-gap, making them good candidates for optoelectronic applications. Their use has thus grown lately, fostered by the need for ever-miniaturized devices, for example in metal oxide semiconductor field-effect transistors[3] in the case of silicon NWs. Another application of the latter is their exploitation to improve solar devices, as described by Yu *et al.*[4], where NWs are used preferably to bulk silicon as they reduce bulk recombination. Besides, thanks to their specific geometry, NWs present less internal defects than bulk materials and a high crystallinity. In contrast, their intrinsically high specific surface area induces more surface defects, which can be interesting for some applications. It has been shown for example that surface defects of ZnO NWs emit in the visible range and in particular in the orange-red wavelengths domain when excited by UV (λ_{exc} lying between 325 and 395 nm)[5,6]. NW arrays can also increase the light extraction efficiency (LEE)[7,8] since (i) they bring more roughness to a surface when deposited on it which induces light scattering, and (ii) they can create a refractive index gradient which favors photons extraction. This property is of great interest to improve the efficiency of light-emitting diodes (LEDs) devices as H. Jeong *et al.*[9] or L. Huang *et al.*[10] highlighted using ZnO nanowires.

Along with NW arrays, other strategies have been developed to improve and to control the light emission of optoelectronic devices. The diffractive properties of periodic structures such as gratings or photonic crystals have been used to both enhance the LEE but also to select the light emission direction[11–14]. Structuring the material on the scale of hundreds of nanometers (corresponding to the emission wavelength in this medium) allows modes trapped in a guiding layer to be efficiently extracted. ZnO NW arrays patterned like a 2D photonic crystals have for example demonstrated a 34% increase in emission intensity of GaN based blue LEDs[15] and have enabled significant enhancement of the luminescence and lasing behavior[16]. Besides this dielectric approach, plasmonic components using metallic nanoparticles[17] or subwavelength periodic structures have also been investigated[18,19]. Using this kind of approach, radiation properties of localized surface plasmon can also help for the light extraction.

Among various possible materials to which the aforementioned structuring strategies could be applied, we have decided to focus our attention on ZnO and derived NW gratings. Indeed, ZnO is an affordable and ecofriendly material with many interesting characteristics

such as a wide-band gap energy of 3.37 eV at room temperature and an exciton binding energy of 60 meV. It is an n-type semiconductor and ZnO NWs find applications in various domains, such as in LED devices as light extraction enhancer as mentioned before[9], photodetectors[20], and to create hydrophobic[21] or super-hydrophobic and self-cleaning surfaces[22]. Recently, ZnO NW gratings have been developed by different processes. The two most common ones are chemical vapor deposition (CVD) and hydrothermal growth. For example, Cheng *et al.*[23] obtained various ZnO nanowire structures, including gratings, by CVD from a patterned photoresist. This approach, although efficient, stays quite expensive and requires devoted equipment. On the contrary, the hydrothermal method is based on growing NWs from a seed layer in a bath containing zinc precursors. This soft chemistry method is less costly and similarly allows to create ZnO NW structures. The grating structures themselves can be obtained by two main methods. One consists in using a template, that can be a pre-patterned gold substrate on which ZnO NWs grow, such as in *Obreja et al.'s* work[24], or an organic sacrificial template[25,26] which is removed afterwards. The other method is based on the direct engraving of the seed layer, by employing a photosensitive zinc-based resist. Park *et al.*[27] used this way to obtain ZnO NW gratings by ultraviolet assisted nanoimprint lithography (NIL). Residual resist between the patterns had then to be removed using a Cl_2 plasma, adding a complex step to the process. Furthermore, derived nanowires had a weak aspect ratio below 5 and/or they grew in the form of disordered flower-like patterns, without any preferential direction.

In this article, we present an original method based on the UV-engraving of a sol-gel ZnO-based photosensitive seed layer combined with hydrothermal growth and leading to dense and rather vertically aligned ZnO NW gratings. The pattern combines both micro- and nano-structuration by using a periodic set of micrometric microcavities made of ZnO NWs. This original structure should benefit both from scattering effect brought by the topographical changes due to the NWs and from the expected diffraction effects due to the presence of the grating. The study of these architectures will be presented in several stages. First, the synthetic protocol to obtain ZnO NW gratings will be detailed, as well as optimization steps of this process. Then, the morphological study of the obtained structures, led by Scanning Electron Microscopy (SEM) and Atomic Force Microscopy (AFM), will be presented. Standard photoluminescence (PL) and angle-resolved photoluminescence (ARPL) results will be shown and discussed. In particular, optical features of ZnO NW gratings will be compared to fully covered ZnO NW samples ("NW coatings"). Electromagnetic simulations were

performed for both kinds of samples to understand the mechanisms involved in their optical behavior and in particular within the multi-scale architectures.

2. Results and discussion

2.1. Optimization of the elaboration process

The localized growth of uniform and reproducible NWs required an accurate control of numerous experimental parameters. For instance, the mask acetone cleaning and O_2 plasma cleaning of the insulated seed layer appeared as essential steps and were preliminarily optimized. Preliminary studies led as well to an optimization of the insulated photoresist development pH and procedure. In the next part, we focus on the optimization of two key parameters that strongly influenced the robustness of our protocol, enabling to obtain uniform, reproducible and tunable ZnO NW gratings. These optimization steps were conducted on (100) silicon wafers.

Using the protocol detailed in the experimental section, individual or aggregated ZnO microrods were frequently observed to pollute the NW gratings, as illustrated in the SEM image of **Figure 1**a. These ZnO rods are characteristic of a homogeneous growth mechanism where particles directly form in suspension in the growth bath according to a mechanism similar to that depicted in Equation 1 but where $Zn(OH)_{(L)}$ react with themselves instead of reacting with $Zn(OH)_{(S)}$. This phenomenon competes with the expected heterogeneous growth mechanism, where the ZnO NWs form on the seed layer. Besides, homogeneous growth partially consumes the zinc precursor in the growth bath, which reduces the precursor amount available for reaction with the seed layer, and thus limits the growth of NWs. Accordingly, very short NWs were observed to grow with a length typically ranging between 200 and 350 nm and a resulting mean grating height of 250 nm, as shown by the AFM profile of Figure 1b.

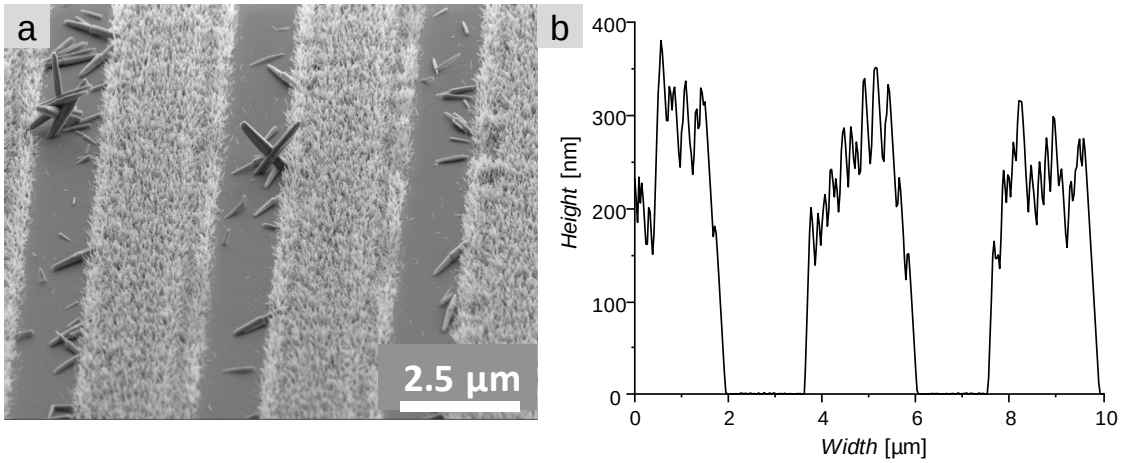

Figure 1: SEM Image showing the coexistence of linear NW gratings and big ZnO rods (a) and AFM profile of resulting gratings (b).

In Figure 1b, the noisy AFM profile shows the NWs constituting the gratings, with a curved grating top that will be explained below. In order to limit the effects of the homogeneous growth, we proceeded to a reduction in the concentration of the zinc precursor in solution from 0.025M to 0.0125M, and we reduced equally the HMTA amount in solution to respect the initial equimolar proportions between Zn and HMTA. The 0.0125M Zn concentration appeared as an ideal trade-off intended to i/ reduce the interaction probability between precursor molecules in solution and thus minimize the homogeneous growth mechanism, and ii/ keep enough zinc precursor in solution available for the heterogeneous growth mechanism. This first optimization proved to be efficient since, as depicted by the two examples illustrated in **Figure 2**, it allowed to get rid of most of the ZnO microrods that polluted the surface and to obtain NW gratings with a consistently enhanced height of 500 to 600 nm. This enhanced height proves that, despite a weaker concentration of ZN in the growth bath, the elimination of the homogeneous growth mechanism leads to an increased amount of Zn precursor available for the NW growth at the seed layer surface.

Another key step of our protocol is the insolation of the photoresist. This step, as detailed in the experimental section, aims at monitoring the chemical reactivity of specific areas of the Zn-BzAc resist so that they can be then selectively etched to obtain grating patterns. In consequence, the insolation power is an important parameter whose influence has been studied and optimized. In preliminary experiments, we observed that, for an insufficient power as well as an excessive one, the resulting NW growth proceeded all over the substrate without considering the insolated gratings pattern (**Figure S1** – see Supplementary Information). We have no clear explanation for both trends, but we make some assumptions. On the one hand, it is possible that a weaker insulating power may not be sufficient to fully activate photo-hydrolysis of the resist, which would result in an ineffective selective etching. On the other hand, we suppose that an excessive power can induce a certain heating of the resist that would be sufficient to chemically stabilize it, again resulting in an ineffective etching in the presently adopted experimental conditions. Accordingly, the best insolation conditions stemmed from a moderate power around 25 mW/cm². Figure 2 illustrates NW gratings obtained after insolation with a power of 23.5 and 25 mW/cm². For both powers, microrod-free and uniformly linear gratings separated by totally denuded stripes of the substrate were obtained. However, this small insolation power difference of 6% leads to significant changes in the features of ZnO NW gratings.

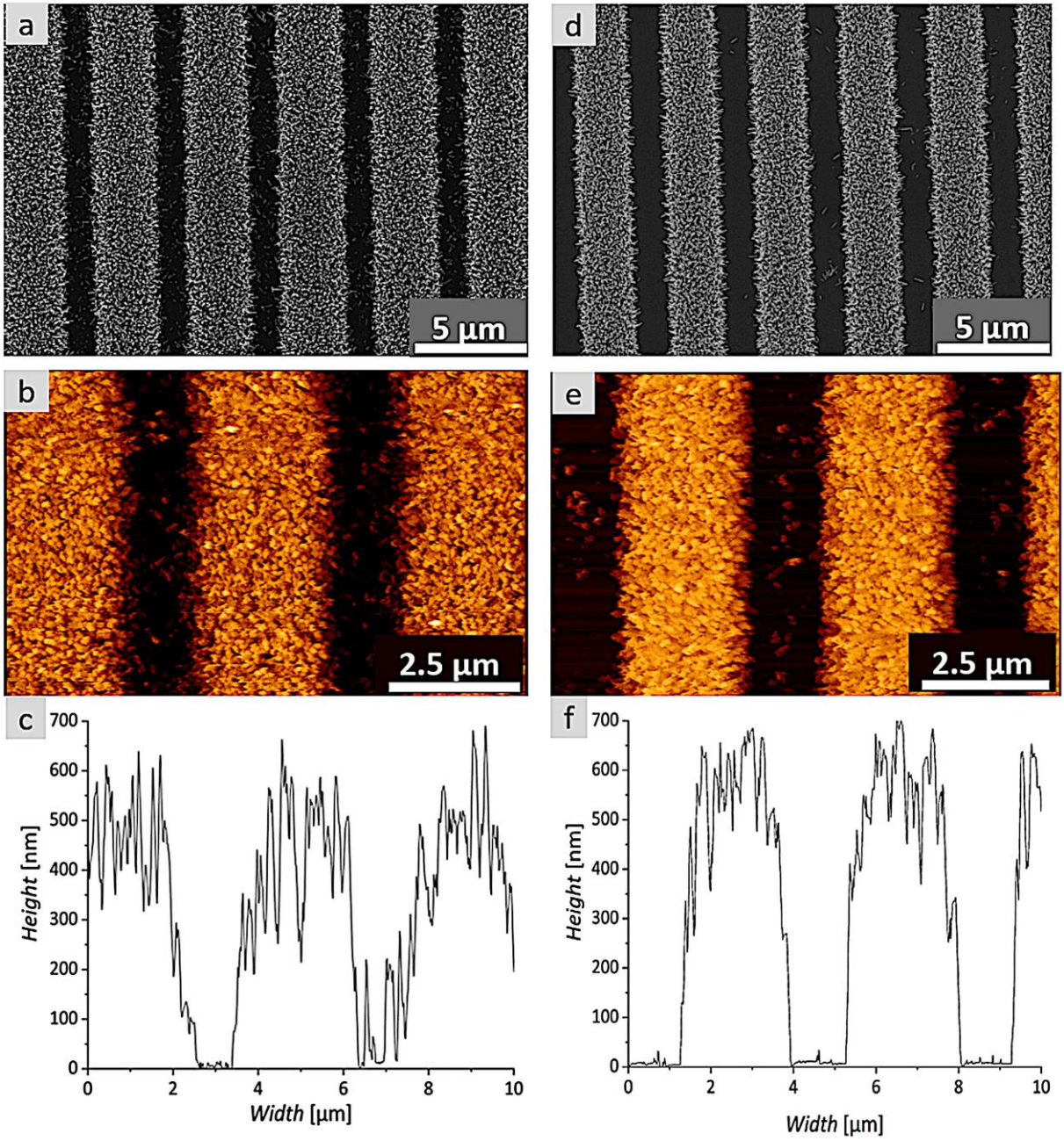

Figure 2: From top to bottom, SEM top view and AFM top view and profiles of ZnO NW gratings on silicon obtained after insolation at a power of 23.5 mW/cm² (a to c) and 25 mW/cm² (d to f).

On the one hand, the AFM profiles indicate a slightly weaker mean grating height for a power of 23.5mW/cm² (around 500 nm – Figure 2c) compared to a 25 mW/cm² one (around 600 nm – Figure 2f). On the other hand, AFM and SEM top view images show that the weaker power leads to significantly wider gratings (around 2.8 µm width) compared to those obtained after an insolation at 25 mW/cm² (around 2.3 µm width). Thus, the higher power apparently results in a grating width much closer to but still greater than the expected one (2 µm according to the mask patterns illustrated in Figure S1 in the Supplementary Information). However, a closer inspection of the grating profile enables to draw further conclusions. **Figure 3**

illustrates SEM cross section images of gratings obtained after insolation at a 25 mW/cm² power. These images highlight the uniformity of NW diameters with a value around 40 nm. It can then be observed that NWs do not grow perfectly vertically, and their inclination tends to increase on the grating edges, leading thus to a kind of reentrant grating profile, similar to a hedgehog. This NW inclination explains the curved top of the gratings, as illustrated by AFM profiles (Figure 1b and Figure 2c & 2f). In particular, according to such reentrant profiles, Figure 3 shows that, for an insulating power of 25 mW/cm², the grating width closely matches the expected value of 2 µm at the NWs-seed layer interface, and this width tends to progressively increase towards the top of the gratings. Such behavior has several practical consequences. It firstly means that AFM and SEM top view images account for the top of the gratings and thus depict a larger width than the expected one. It also means that, since the AFM tip cannot reliably probe structures with reentrant profiles, AFM profiles shown in Figure 1b and Figure 2c & 2f do not rigorously account for the real grating profile. These features highlight therefore that, in the frame of this work, AFM and SEM characterizations provide useful complementary information. The former enables to precisely quantify the NW lengths and grating heights while the latter enables to reliably probe the exact grating profile. According to all these considerations, the insulating power was definitely set to 25 mW/cm² in following studies.

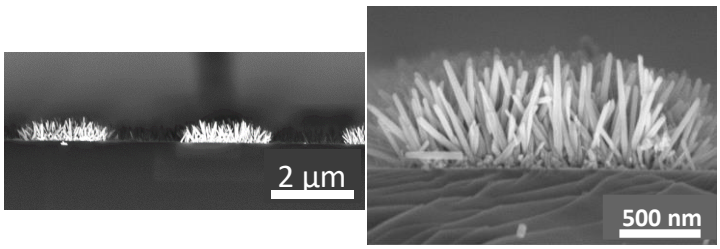

Figure 3: SEM cross section images of ZnO NW gratings on silicon obtained after insolation at a 25 mW/cm² power.

To assess the robustness of our optimized protocol, we studied the uniformity and reproducibility of NW grating on the surface of 3x3 cm^2 Si wafers. The photograph of **Figure 4**a depicts uniform diffraction features which provide first evidence that NW gratings have been elaborated in a homogeneous way on the whole substrate surface. This homogeneity is clearly illustrated by the SEM image at low magnification of Figure 4b. The high magnification SEM top view of Figure 4c shows that the gratings are constituted of uniformly distributed NWs whose density at the grating top has been approximately determined to be 190 NWs/µm². **Figure 5** illustrates a SEM top view mapping of gratings elaborated on the entire surface of a 3x3 cm^2 Si wafer. As previously explained, such SEM data do not directly account for the real grating width, but they provide a reliable assessment of the grating

uniformity. Accordingly, the mapping of Figure 5 shows reproducible gratings all over the substrate surface with a width (near the grating top) of 2.1 +/- 0.2 µm. These features enable us to definitively conclude that our protocol is robust.

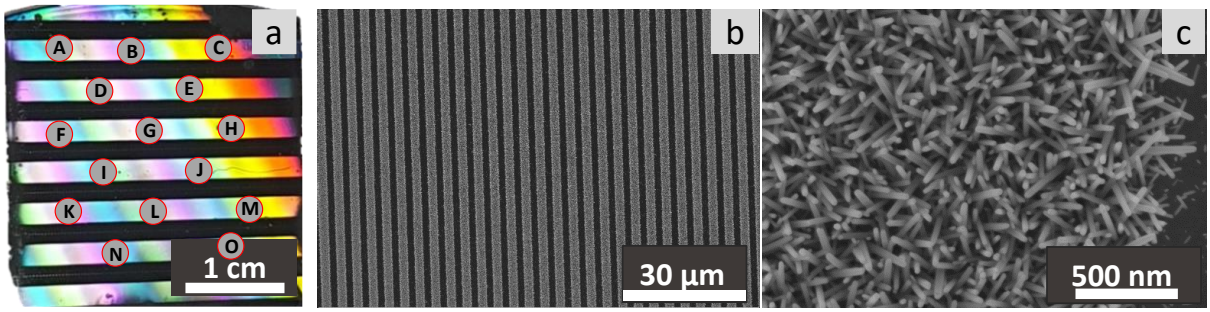

Figure 4: Large scale photograph (a) and SEM images at low (b) and high (c) magnifications of NW gratings elaborated on 3x3 cm^2 Si wafers after insolation at a 25 mW/cm^2 power. In the photo, the 15 areas noted A to O indicate where SEM images of Figure 5 have been considered.

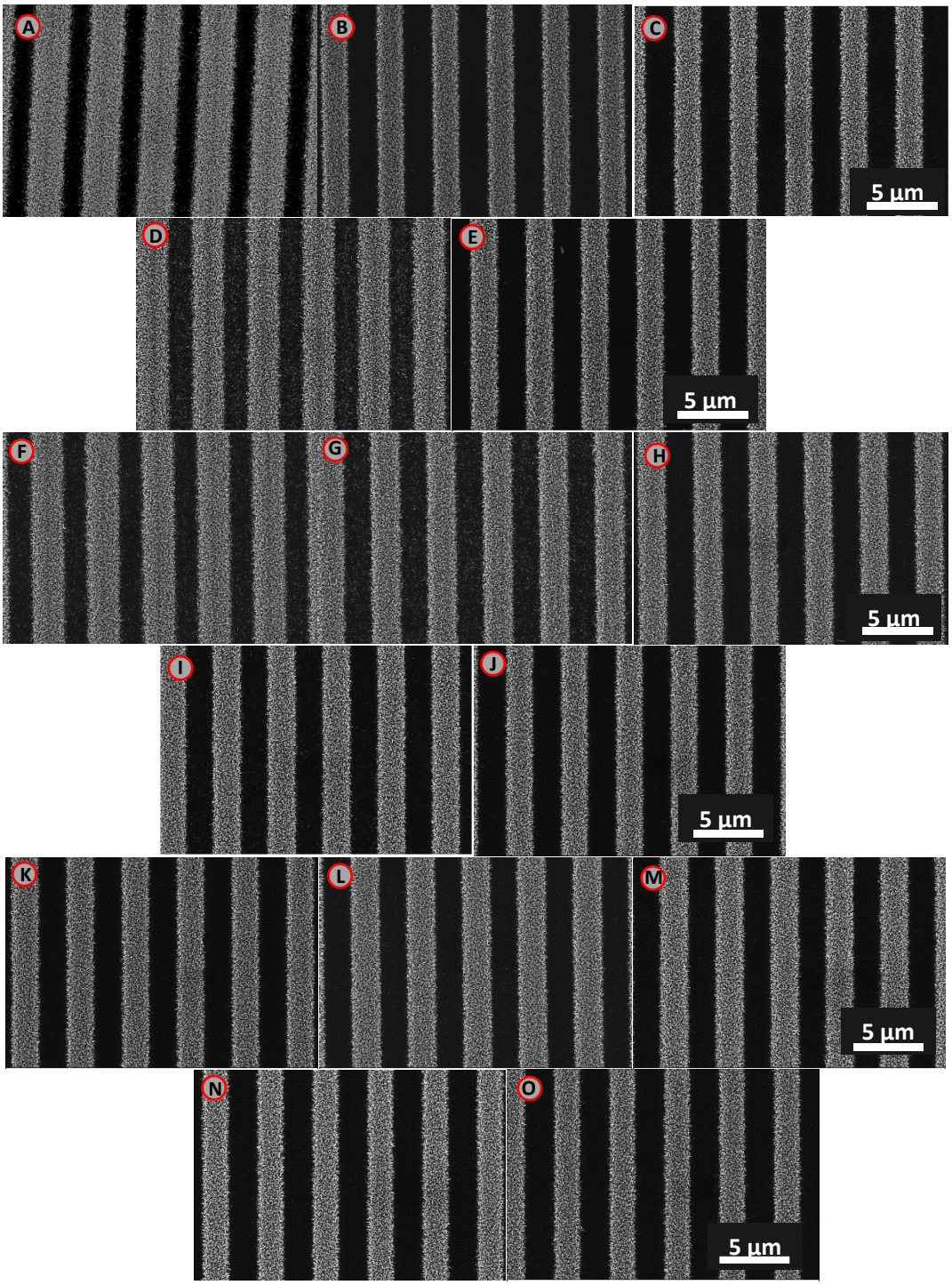

Figure 5: SEM top view mapping of ZnO NW gratings on a 3x3 cm^2 Si wafer obtained after insolation at a 25 mW/cm^2 power. The localization of areas A to O is depicted in Figure 4a.

This protocol, thoroughly optimized on Si wafers, has then been successfully extrapolated to quartz and glass substrates, which present numerous interests for optical applications. In the following, we focus on quartz substrates that will be then exploited in the frame of optical characterizations. The main grating features on 2.5x2.5 cm^2 quartz substrates are summarized in **Figure 6**. Globally speaking, this figure illustrates identical features as those previously depicted on silicon substrates, *i.e.* similar homogeneous diffraction effects at the macroscopic

scale, uniformly linear gratings with a width and mean height near to those obtained on silicon, as well as a comparable NW diameter around 45 nm. Only some minor differences have been identified through the analysis of SEM data, namely a weaker NW density of about 160 NWs/µm². Such minor differences, which may arise from the chemical nature and/or topology of the substrate, have not yet been clearly explained.

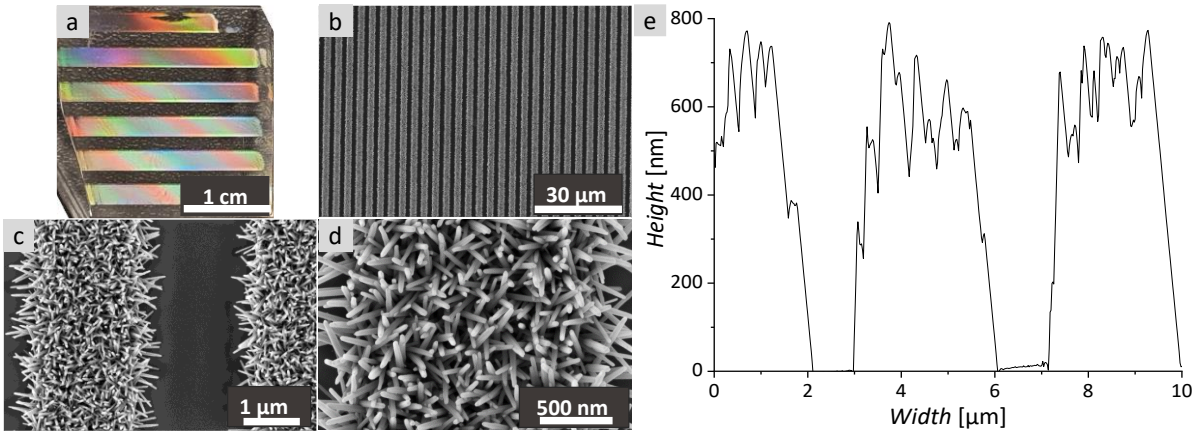

Figure 6: ZnO NW gratings on 2.5x2.5 cm^2 quartz substrate illustrated by macroscopic photography (a), low (b) to high magnification (d) SEM images, and AFM profile (e).

2.2. Optical characterizations

To thoroughly study the optical properties of the elaborated ZnO NW structures, ARPL spectra were recorded at room temperature (300 K) for both ZnO NW coatings (full coverage) and ZnO NW gratings. These emission spectra were recorded with a backside excitation source emitting at 375 nm and the angle of the detector varied from 0° (source and detector were aligned on each side of the sample) to 90° (detector on the edge of the sample, perpendicular to the source – see Figure S2 in the Supplementary Information). Characteristic emission profiles of these samples recorded at 0° are presented in **Figure 7**. Both spectra exhibit a large emission band between 400 and 800 nm, centered around 600 nm, in the orange-red spectral range. This large emission band has already been reported in the literature and is explained by radiative recombination processes caused by defects (oxygen and zinc vacancies) on the surface of the nanowires [5,6,31]. It should be noted that several spurious emission signals attributed to the experimental set-up (at 750 nm: second order of the excitation source –λ_{exc}=375 nm, and other signals linked to the set-up) are also observed between 750 and 900 nm. Another set-up has also been used to record emission spectra on the same samples, exciting them from the front at a fixed angle of 45°. The corresponding spectra are gathered in **Figure S2** with a description of the set-up (Supplementary Information): they only present a large emission band lying from 400 to 800 nm, without the afore observed spurious signals, confirming these latter are due to the ARPL set-up.

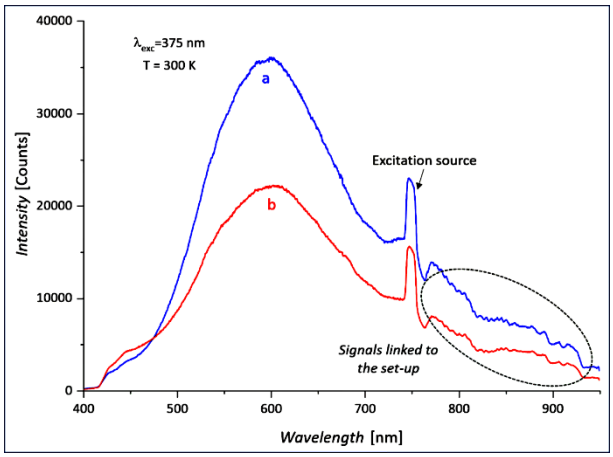

Figure 7: Room-temperature emission spectra recorded using a backside excitation at 375 nm on (a) a ZnO NW coating (full coverage) and (b) a ZnO NW grating grown on quartz.

The evolution of emission intensity as a function of wavelength and detection angle has been plotted for both kinds of samples. Resulting luminescence maps are gathered in **Figure 8**. A quick glance shows a very significant influence of the grating (Figure 8b) as its emission intensity is strongly enhanced in a specific angular range between 60 and 70° whereas the full-covered sample (Figure 8a) is characterized by a strong emission intensity that changes little for a detection angle lying between 0 and 50°. A significant increase in emission intensity can be noticed at high angles (above 85°).

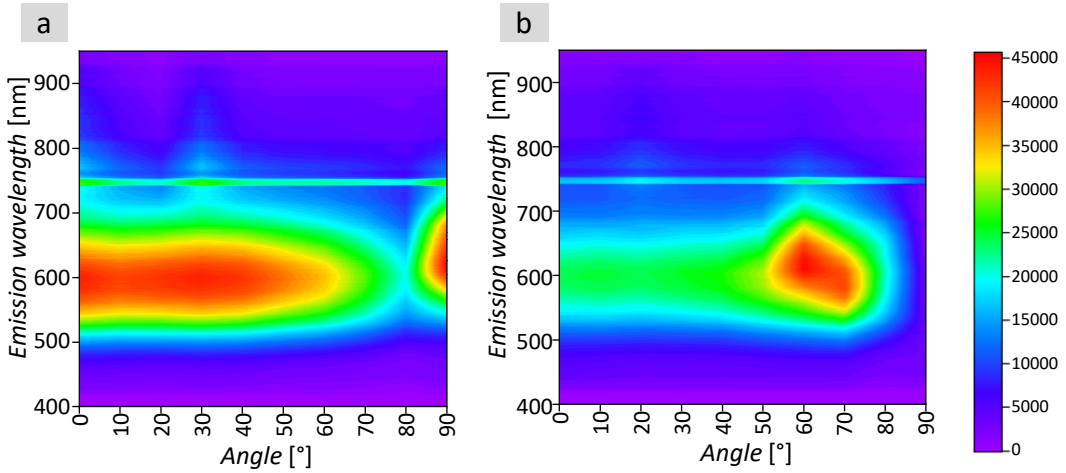

Figure 8: Room temperature ARPL map showing the evolution of the emission intensity with the wavelength and detection angle for (a) the ZnO coating and (b) the ZnO grating under 375 nm excitation

To facilitate the interpretation of these results, we have plotted the photoluminescence intensity at 600 nm versus the emission angle (**Figure 9**). The main trends identified on the Figure 8 are confirmed. Accordingly, the emission of the ZnO NWs coating as a function of the observation angle (Figure 9a) shows an almost constant emission intensity around 600 nm between 0° and 50°. The intensity decreases then with further increase in the emission angle, losing about 50% of its value at 80°. Beyond 80°, we observe a noticeable increase in the

emission intensity that reaches values comparable to the initial emission (below 50°) for angles greater than 85°. The strong intensity measured between 85 and 90° is explained by the extraction of guided photons trapped into the ZnO NW coating and perhaps into the quartz substrate[32].

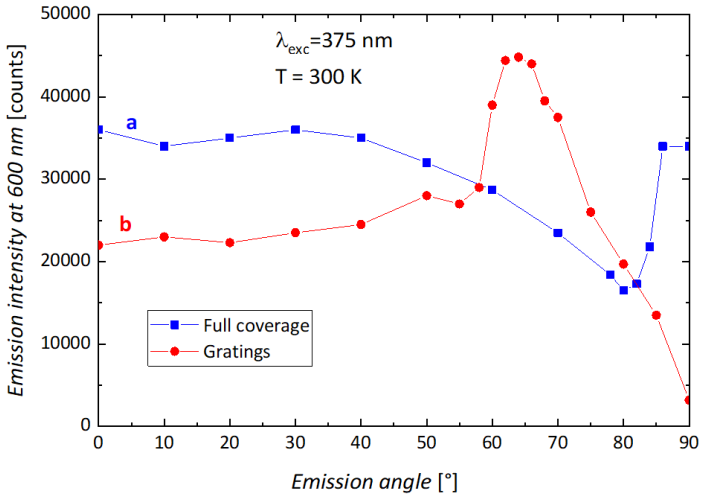

Figure 9: Angle dependent emission intensity (λ_{em}=600 nm, backside excitation at 375nm and 300K) for (a) a ZnO NW coating and (b) a ZnO NW grating.

In contrast, the grating structuring significantly modifies the emission. As highlighted by the Figure 9b, the emission is rather constant between 0° and 40°, and, in this angular domain, it is approximately 40% weaker than for the full-covered sample. This result is partly justified by the quantity of emitting centers being twice as low for the gratings. As already illustrated in Figure 8, the main changes brought by the grating structuring are observed at greater angles where the emission intensity is observed to strongly increase and to reach a value about twice greater than the initial one for angles between 60° and 70°. Beyond 70°, we observe a continuous decrease in intensity leading to a minimum value, almost 7 times lower than the value at 0°, for an angle of 90°. These results clearly demonstrate that the grating structure allows a light extraction enhancement of the guided modes leading to an emission intensity increase for emission angles around 60-70°. Over this angular range, there is therefore a strong enhancement of the luminescence emission of the ZnO NW gratings, largely exceeding the maximum emission intensity of the full covered sample while there are only half as many emitting centers.

To study more precisely the emission behavior induced by the presence of the gratings, an enhancement factor has been determined by dividing the emission spectrum data obtained at a fixed angle by those of the spectrum recorded at 0°. This enhancement factor is plotted as a function of wavelength for angles between 50 and 70° (**Figure 10**). For an angle of 50° (in

black), the spectrum presents a profile similar to the classical emission spectrum with a large maximum intensity centered around 600 nm, which reflects an overall increase in emission intensity over the entire range of wavelengths without changing the spectral profile.

This is not the case for greater emission angles where the enhancement factor exhibits a significant asymmetry. This later is particularly marked at 58° (in purple) and 60° (in dark blue) where the light extraction due to the grating is favored in the red region, and the emission enhancement factor is maximum around 700 nm at 58°. Then, when increasing the emission angle, the asymmetry of the enhancement factor progressively disappears and the maximum gain shifts towards the lower wavelengths, from 700 nm for 58° to about 575 nm for 70°. The most homogeneous gain is obtained for an angle of 62° (in bright blue) in a wide range of wavelengths (500-750 nm).

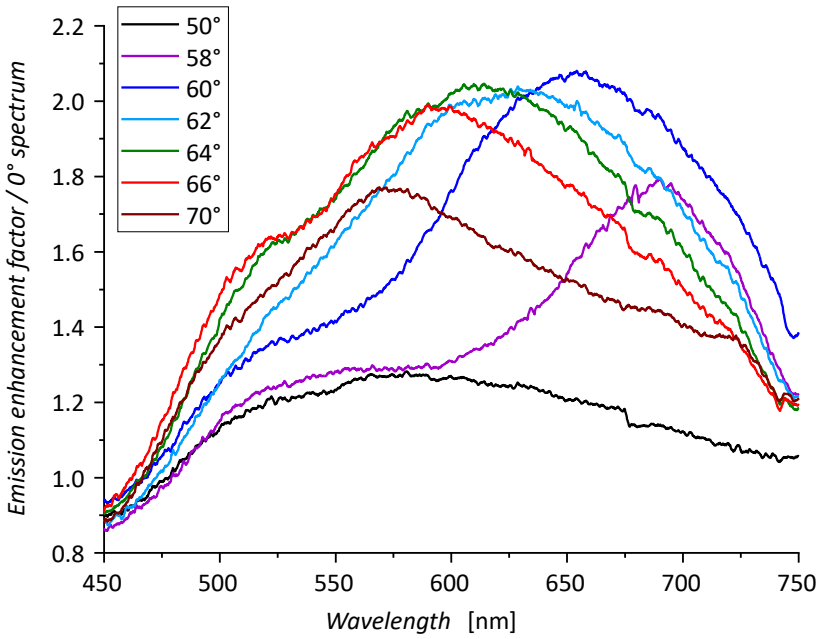

Figure 10: Emission enhancement factor compared to the spectrum at 0° versus emission wavelength for angles between 50° and 70°, measured on a sample containing ZnO NW gratings.

This study thus shows that, for some angles, the grating structure makes it possible to enhance specific wavelengths that do not necessarily correspond to the emission maximum intrinsically due to the NWs. This complex behavior, together with the strong intensity enhancement of photoluminescence observed in Figure 8 and Figure 9, suggest the presence of a resonant electromagnetic mode within the grating structure.

The experimental dispersion curve is obtained by monitoring the angular position of PL emission peaks for a set of wavelengths between 580 nm and 700 nm. To draw it, the wavelength corresponding to the intensity peak is plotted as a function of the wavenumber

$k_x = k_0 sin\theta$ expressed in $\frac{2\pi}{D}$, where $k_0 = \frac{2\pi}{\lambda}$ and D is the grating period (**Figure 11**). The error bars correspond to the measurement uncertainty of 1° for the emission angle θ.

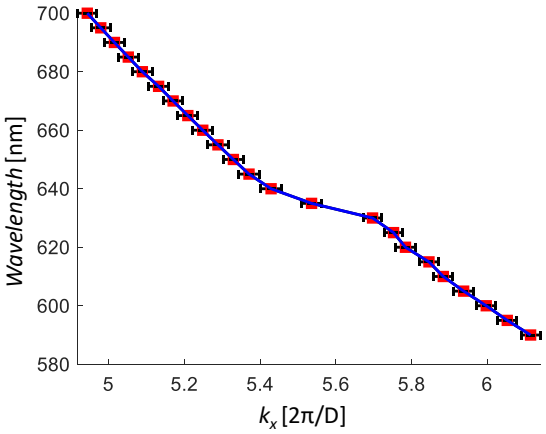

Figure 11: Experimental dispersion relation obtained from angle-resolved PL data.

This dispersion curve highlights the presence of an electromagnetic mode responsible for the enhancement of the PL in the red part of the visible spectrum.

2.3. Simulations

To understand the origin of the enhancement of PL produced by the grating, we considered a bidimensional problem depicted in **Figure 12**. Since the set of NWs present a complex random spatial distribution, we replaced the ZnO NWs by a homogeneous medium of refractive index n_h. This refractive index is estimated using a Maxwell-Garnet homogenization formula[33] :

$$n_h = [f n_{ZnO}^2 + (1-f) n_0^2]^{0.5} \qquad \text{(Equation 1)}$$

where n_{ZnO} and n_0 are the refractive indices of ZnO and air, respectively, and f is the filling factor of ZnO. In two dimensions, f is about 0.57 for a NW density around 200 NW/μm^2 and for a NW diameter of ~40 nm. Considering that the optical index of ZnO is close to 2 in the visible range, n_h is approximately equal to 1.65, higher than that of the quartz substrate (1.45). This model enables us to determine the dispersion relation of the modes propagating within the ZnO coating layer whose thickness has been set to 600 nm. We found two modes for both TE (Transverse Electric) and TM (Transverse Magnetic) polarization cases (see the paragraph SI.3 and **Figure S3** placed in the Supplementary Information). The fundamental modes present similar effective indices which are higher than those of the second antisymmetric-like modes (see Figure S3). Here, we focus on the fundamental one whose wavenumbers is denoted $\beta = k_0 n_{\text{eff}}$. Its effective index n_{eff} is almost nondispersive and close to 1.6. This result confirms that the ZnO NWs coating supports guided modes responsible for the emission recorded around 90° (see Figure 8a or Figure 9a).

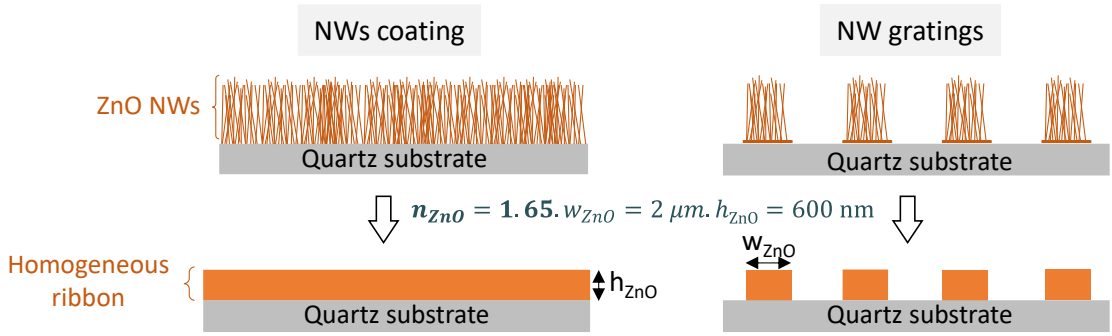

Figure 12: Schematic representation of the modeling of ZnO NW coating and grating by solid blocks. The main parameters used are noted in the center of the figure.

The grating structure can therefore be considered as a periodic set of truncated waveguides. Each finite length waveguide forms a cavity of width W, which has its own resonances built by the guided modes that interfere constructively. These resonances can be caught by a simple Fabry-Perot model[34] whose reflection coefficient is given by:

$$r = \frac{\rho(1-e^{2i\beta W})}{(1-\rho^2 e^{2i\beta W})} \qquad \text{(Equation 2)}$$

where ρ is the Fresnel coefficient. The resonances can be found by calculating the poles $\widetilde{\omega}$ in the complex plane of the reflection coefficient (see SI.4). The real part of the poles corresponds to the resonant angular frequencies while the imaginary part is related to the quality factor Q of the cavity (being ratio of the stored energy to the energy dissipated per oscillation cycle). The analytical calculations of the poles give:

$$\lambda_{(q)} = \frac{2n_{eff}W}{q} \qquad \text{(Equation 3)}$$

$$Q_{(q)} = -q\frac{\pi}{2\ln|\rho|} \qquad \text{(Equation 4)}$$

where q is the resonance order. For a ribbon of width $W = 2$ µm, three resonant wavelengths are found in the spectral range of the PL emission, 585 nm, 643 nm and 714 nm for q equal 11, 10 and 9, respectively, whose quality factors are around 11. This demonstrates that photons emitted by the ZnO NWs are trapped and constructively interfere within the ribbons, explaining the enhancement of the PL for ZnO NW gratings. Note that we could even expect larger Q factors since the ribbons are bidimensional cavities that better trap the photons. However, the electromagnetic coupling between adjacent ribbons must be considered to improve this simple image. For that purpose, we have calculated the dispersion relation of the grating using a finite element method implemented in the COMSOL Multiphysics software. We found that the best agreement between the simulated and experimental dispersion relations occurs for a reduced ribbon width of 1.6 µm, instead of 2 µm according to the used mask. Similar dispersion relations were obtained for both TE and TM polarized light and only

the eigenmodes presenting Q factors larger than 10 have been plotted (**Figure 13**). The reduced ribbon width introduced here can be considered as an effective width that takes into account the decrease in NW density at the periphery of the ribbons. Experimental and simulated dispersion relations fit very well. Note that a symmetric experimental dispersion curve could be added by scanning the PL emission for negative detection angles. We also observed that the quality factor ranges between 17 to 26 which is larger than that obtained by the simple 1D Fabry-Perot model (around 11 as mentioned before), showing the stronger localization effect allowed by 2D cavities. The electromagnetic coupling between the ribbons slightly shifts the resonant wavelengths and lifts the degeneracy of the modes at the edge of the Brillouin zone.

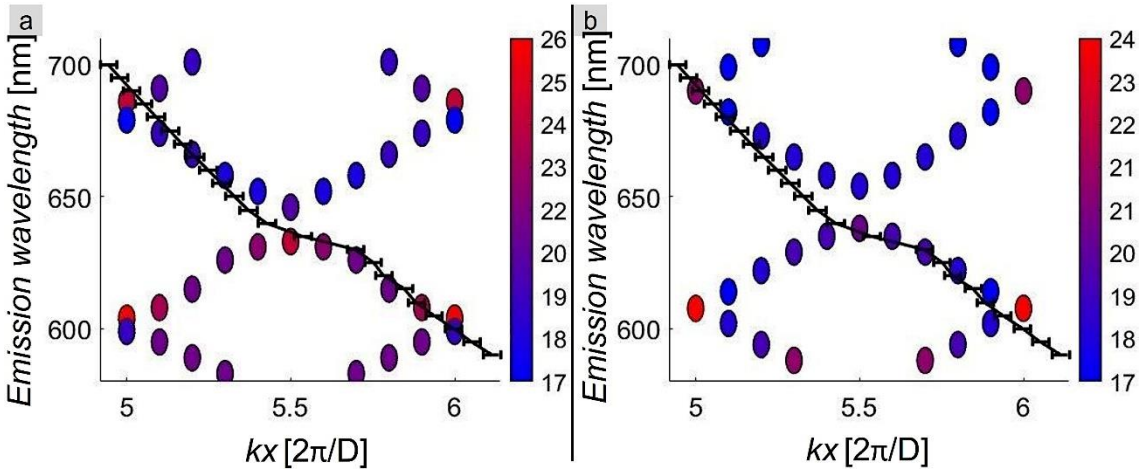

Figure 13: Colored circles: (a) and (b) are the theoretical dispersion relation for TE and TM polarizations, respectively, computed for ribbons of 1.6 µm width, 600 nm height, and 4 µm grating period. The value of the quality factor corresponds to the color of the circles. The black curve is the experimental dispersion relation.

Although the emitted photons could be radiated by several diffraction orders of the grating, we have experimentally observed that the enhanced PL emission occurs only for angles lying from 50° to 70°. The selection of the fifth and sixth diffraction orders is explained by the phase matching condition between the guided modes and the radiated plane waves[35]. Assuming that the wavenumber of the guided modes within the ribbons made of NWs is close to that for the infinite waveguide, the Bragg scattering condition leads to:

$$k_x \approx \beta - p2\pi/D \qquad \text{(Equation 5)}$$

where p is an integer. The diffraction angles are then approximatively obtained by:

$$sin\theta_p \approx n_{eff} - p\lambda/D \qquad \text{(Equation 6)}$$

Since the effective index of the guided mode is larger than 1.6 for TE and TM polarized light (see Figure S3 in the Supplementary Information), the first diffraction order that satisfies

Equation 6 corresponds to the fifth diffraction order explaining that the enhanced PL is collected for $k_x \in [5,6]\frac{2\pi}{D}$.

These conclusions are confirmed by the electromagnetic simulations that allow us to compute the map of electric field of the eigenmodes and their radiated power in the far-field. For example, at 604 nm and for a TE polarized light, the electric field resonates within the ZnO ribbon (**Figure 14**a). The electric field inside the ribbon corresponds to the fundamental mode of the infinite waveguide (guided within the ZnO coating, **Figure S4** – see Supplementary Information) showing that the resonance mechanism can only be attributed to the fundamental guided mode since the antisymmetric one plays a negligible role because of its low Q factor. The near field map (Figure 14a) also shows a large amount of electric field outside the ribbon, highlighting the strong electromagnetic coupling with its neighbors. Lastly, the angular distribution of the far-field intensity shows that the emission is coupled out at 60° and at the symmetric direction (300°), Figure 14b.

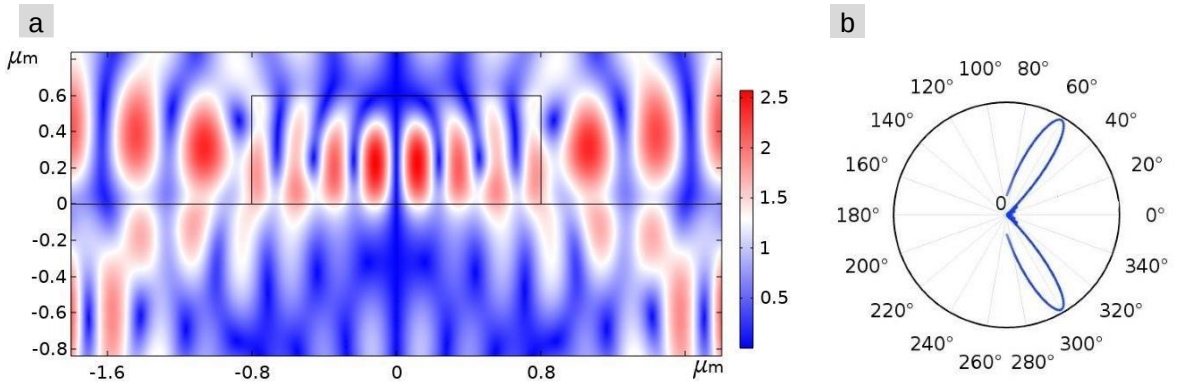

Figure 14: (a) Map of the modulus of the electric field (for TE polarization) in the near field at 604 nm for $k_x = 6\frac{2\pi}{D}$. (b) Angular representation of the far field intensity (in a.u.) of the eigenmode.

The established effective model thus explains that the photoluminescence enhancement originates from both coupled cavity resonances and a diffraction mechanism that enable the extraction of the resonant photons towards some specific angles.

3. Conclusion

In this work, we have presented an original way to elaborate luminescent ZnO NW-based architectures. A sol-gel derived Zn-BzAc photoresist has first been deposited by spin-coating on silicon or quartz substrate. After crystallization at 540°C, this resist serves as seed layer for the subsequent growth of ZnO NWs by hydrothermal synthesis at ambient pressure. This procedure allows the elaboration of samples with NWs fully covering the substrate (NWs coating); using a preliminary selective insolation of the photoresist leads to samples constituted of NW gratings. On the basis of SEM and AFM characterizations, we have firstly

shown how the optimization of key experimental parameters, in particular the precursor concentration in the bath used for NW growth and the light power during the resist insolation step, enables the implementation of a robust protocol leading to uniform and reproducible NW linear and periodic gratings with a width / pitch of 2 µm / 4 µm. Optimized conditions have been defined as a zinc precursor concentration in solution of 0.0125M and an insolation power of 25 mW/cm². Derived NW coating and grating-constituted samples have then been thoroughly characterized by standard PL and ARPL measurements. Former optical characterizations show that, under UV excitation (375 nm), both kinds of samples similarly emit light in the orange-red spectral range (around 600 nm), which is attributed to radiative transitions induced by structural defects at the ZnO NWs surface. In contrast, ARPL intensity measurements and mapping demonstrate that light emission is considerably influenced by the presence of NW gratings, that strongly enhance the extraction of light emitted by the ZnO NWs and trapped as guided modes into the NW layer in the case of a full covered sample. This enhancement proceeds in a selective range of emission angles, between 50 and 70°. More specifically, for angles lying in the 58-62° range, the grating structure makes it possible to exalt specific wavelengths in the red spectral range (up to 700-750 nm) that are largely exceeding the emission wavelength intrinsically due to the NWs. Electromagnetic simulations have then been performed to explain these features. For that purpose, an effective model has been developed where the complex random spatial distribution of NWs is simulated by a homogeneous medium. A good agreement between the theoretical dispersion relation derived from this model and the experimental one enables to validate the suggested model. This latter finally allows proposing a phenomenological and quantitative description showing the role of microcavities played by the ZnO NW gratings. In this description, the PL emission is boosted thanks to coupled cavity resonance phenomena together with a diffraction mechanism, which (i) enables the extraction of the resonant photons towards some specific angles and at given wavelengths, and (ii) supports experimental results arising from PL measurements. These specific features could be put to good use in applications where specific spatial extraction is useful such as anti-counterfeiting marking. Other gratings configurations have to be studied to better apprehend the influence of gratings parameters on the aforementioned phenomena.

4. Experimental Section/Methods

Elaboration of ZnO nanowires

The elaboration of ZnO nanowire gratings was performed through hydrothermal growth from a previously deposited crystalline ZnO seed-layer. This last one is originated from a sol-gel

based procedure that was previously established in our group.[28] The sol is constituted of 0.36M of zinc acetate dehydrate (ZAD) and monoethanolamine (MEA) in equimolar quantities, and diluted in 1-butanol. It was then aged by stirring at 90°C for 3 hours before use. In the case of gratings, this process has been adapted from the work of Kawahara *et al.*[29,30] in order to obtain a positive photoresist, *i.e.* that directly reproduces the pattern of a chromium mask.-The adaptation consisted in the addition of benzoylacetone (BzAc, 0.34M) to the sol before the aging process. Benzoylacetone forms chelation rings with zinc, which leads to a stable Zn-BzAc resist when immersed in acidic solution. In contrast, the chelate is chemically destabilized by photo-hydrolysis when exposed to UV irradiation, and the resist can be removed from the substrate by dilution in acidic medium. It allows thus its local elimination after selective UV exposition through a chromium mask.

The so-obtained Zn-BzAc photosensitive sol was deposited by spin-coating a 300 µL droplet for 10s at 3000 rpm on 3x3 cm² (100) silicon wafers and 2.5x2.5 cm² quartz substrates. It was then dried and partially stabilized at 110°C for 30 min in an oven before being introduced in an UV-insolation device (UV-KUB from KLOE Company) operated at a 365 nm wavelength. For the selective insolation we used a quartz mask with chromed linear gratings of 2 µm / 4 µm width / pitch as illustrated in Figure S1 (Supplementary Information), and the insolation was performed for 40 min.

After insolation and a short post-baking at 110°C for 8 minutes, the sample was dipped for 30 s in a development bath of nitric acid at pH=3 in order to etch the insolated parts of the photoresist and to reveal the grating patterns. After subsequent washing with deionized water and drying with nitrogen flow, it was then annealed for 1 hour at 540°C to form a crystalline ZnO seed-layer structured in the form of linear gratings separated by denuded stripes of the substrate.

For the NW growth step, we also used a protocol developed in our group[28]. A growth bath constituted of an equimolar aqueous solution of hexamine (HMTA) and zinc nitrate (ZN) was prepared and heated at 90°C. The concentration of both chemicals was initially fixed at 0.025M, and further optimization will be described below. The seed-layer coated substrate was cleaned with an O_2 plasma (12V, 3min) before being attached to a home-made PTFE sample holder, facing down and inclined at 45° to limit the deposition of pollutants arising from homogeneous growth in the liquid medium. Then, it was dipped for 30 min in the growth bath stirred at 500 rpm. This operation led to the localized hydrothermal growth of the nanowires on the structured seed-layer according to Equation 6, where $Zn(OH)_{(L)}$ represents

the reactive species in solution and $Zn(OH)_{(S)}$ the reactive species at the surface of the substrate.

$$Zn(OH)_{(L)} + Zn(OH)_{(S)} \rightleftharpoons ZnO_{(s)} + H_2O \qquad \text{Equation 6}$$

The sample was then washed with deionized water and subsequently dried with a nitrogen flow. It resulted in the elaboration of NW gratings according to an original procedure never reported before to our knowledge.

Characterization techniques

Morphological features of ZnO NWs were mainly studied by SEM and AFM. The complementarity of both methods used to assess the NW gratings will be analyzed below. The SEM employed was a ZEISS Gemini300 operated with a voltage of 3 kV and using an in-lens detector at a working distance of 6 mm. For the AFM, we used a JPK Nanowizard 4 with OTESPA probes. The emission properties of the samples were measured at room temperature using standard and ARPL set-up. The second harmonic (375 nm) of a Ti:sapphire laser was used to illuminate the sample from the backside of quartz substrates supporting ZnO nanowires. The PL signal was detected by an optical fiber mounted on a goniometer to collect emission from 0°, *i.e.* perpendicularly to the substrate, to 90° with an angular resolution of 0.6°. The signal was then focused on the slit of a 32 cm focal monochromator and detected by a CCD camera (Figure S6, placed in Supplementary Information, presents a scheme of the set-up).

Electromagnetic simulations

The dispersive properties of the ZnO NW gratings were calculated with a finite element method implemented in COMSOL Multiphysics. We simulated a unique cell with boundary conditions in the periodic directions of the grating and perfect matched layers (PML) in the perpendicular directions. The eigenmodes and complex eigenfrequencies were computed for the Bloch wavenumber lying in the first Brillouin zone. The quality factor and resonant wavelengths were derived from these eigenfrequencies.

Supporting Information

Supporting Information is available from the Wiley Online Library.

Acknowledgements

This work was financially supported by the French “Agence Nationale de la Recherche” in the frame of the ANR SMARtLEDs project (ANR-19-CE08-0001).

Received: ((will be filled in by the editorial staff))
Revised: ((will be filled in by the editorial staff))
Published online: ((will be filled in by the editorial staff))

References

[1] M. Liu, P. Jin, Z. Xu, D. A. H. Hanaor, Y. Gan, C. Chen, *Theoretical and Applied Mechanics Letters* **2016**, *6*, 195.
[2] S. Alagha, A. Shik, H. E. Ruda, I. Saveliev, K. L. Kavanagh, S. P. Watkins, *Journal of Applied Physics* **2017**, *121*, 174301.
[3] H. Zhu, in *Nanowires - New Insights* (Ed.: K. Maaz), InTech, **2017**.
[4] P. Yu, J. Wu, S. Liu, J. Xiong, C. Jagadish, Z. M. Wang, *Nano Today* **2016**, *11*, 704.
[5] K. Chen, D. D. Thang, S. Ishii, R. P. Sugavaneshwa, T. Nagao, *Opt. Mater. Express* **2015**, *5*, 353.
[6] N. Zhou, B. C. Hu, Q. Y. Zhang, C. Y. Ma, S. Z. Hao, *AIP Advances* **2019**, *9*, 045004.
[7] S.-Y. Hsu, M.-C. Lee, K.-L. Lee, P.-K. Wei, *Appl. Phys. Lett.* **2008**, *92*, 013303.
[8] M. Djavid, Z. Mi, *Appl. Phys. Lett.* **2016**, *108*, 051102.
[9] H. Jeong, D. J. Park, H. S. Lee, Y. H. Ko, J. S. Yu, S.-B. Choi, D.-S. Lee, E.-K. Suh, M. S. Jeong, *Nanoscale* **2014**, *6*, 4371.
[10] L. Huang, F. Zhang, D. Yuan, B. Liu, C. Cheng, *Physica E: Low-dimensional Systems and Nanostructures* **2022**, *142*, 115326.
[11] N. Ganesh, W. Zhang, P. C. Mathias, E. Chow, J. A. N. T. Soares, V. Malyarchuk, A. D. Smith, B. T. Cunningham, *Nature Nanotech* **2007**, *2*, 515.
[12] K. McGroddy, A. David, E. Matioli, M. Iza, S. Nakamura, S. DenBaars, J. S. Speck, C. Weisbuch, E. L. Hu, *Appl. Phys. Lett.* **2008**, *93*, 103502.
[13] J. J. Wierer, A. David, M. M. Megens, *Nature Photon* **2009**, *3*, 163.
[14] J. H. Lin, C.-Y. Tseng, C.-T. Lee, H.-C. Kan, C. C. Hsu, *Opt. Express* **2013**, *21*, 24318.
[15] H. Park, K.-J. Byeon, K.-Y. Yang, J.-Y. Cho, H. Lee, *Nanotechnology* **2010**, *21*, 355304.
[16] C. Zhang, X. Huang, H. Liu, S. J. Chua, C. A. Ross, *Nanotechnology* **2016**, *27*, 485604.
[17] M. Khaywah, A. Potdevin, F. Réveret, R. Mahiou, Y. Ouerdane, A. Désert, S. Parola, G. Chadeyron, E. Centeno, R. Smaali, A. Moreau, *J. Phys. Chem. C* **2021**, *125*, 7780.
[18] K.-G. Lee, K.-Y. Choi, S.-H. Song, *Current Applied Physics* **2014**, *14*, 1771.
[19] G. Lozano, S. R. Rodriguez, M. A. Verschuuren, J. Gómez Rivas, *Light Sci Appl* **2016**, *5*, e16080.
[20] B. A. Albiss, M.-A. AL-Akhras, I. Obaidat, *International Journal of Environmental Analytical Chemistry* **2015**, *95*, 339.
[21] A. Singh, S. Singh, *Bull Mater Sci* **2018**, *41*, 94.
[22] H. H. Tran, R. B. Venkatesh, Y. Kim, D. Lee, D. Riassetto, *Nanoscale* **2019**, *11*, 22099.
[23] C. Cheng, M. Lei, L. Feng, T. L. Wong, K. M. Ho, K. K. Fung, M. M. T. Loy, D. Yu, N. Wang, *ACS Nano* **2009**, *3*, 53.
[24] P. Obreja, D. Cristea, A. Dinescu, C. Romaniţan, *Applied Surface Science* **2019**, *463*, 1117.
[25] M. Maddah, C. P. Unsworth, N. O. V. Plank, *Mater. Res. Express* **2018**, *6*, 015905.
[26] G. P. Papageorgiou, A. G. Karydas, G. Papageorgiou, V. Kantarelou, E. Makarona, *Micro and Nano Engineering* **2020**, *8*, 100063.
[27] H.-H. Park, X. Zhang, K. W. Lee, K. H. Kim, S. H. Jung, D. S. Park, Y. S. Choi, H.-B. Shin, H. K. Sung, K. H. Park, H. K. Kang, H.-H. Park, C. K. Ko, *CrystEngComm* **2013**, *15*, 3463.
[28] T. Demes, C. Ternon, D. Riassetto, V. Stambouli, M. Langlet, *J Mater Sci* **2016**, *51*, 10652.
[29] T. Kawahara, T. Ishida, H. Tada, N. Tohge, S. Ito, *JOURNAL OF MATERIALS SCIENCE LETTERS* **2002**, *21*, 3.
[30] T. Kawahara, T. Ishida, H. Tada, N. Noma, N. Tohge, S. Ito, *JOURNAL OF MATERIALS SCIENCE LETTERS* **2003**, *38*, 5.
[31] N. Amara, A. Martin, A. Potdevin, D. Riassetto, M. Messaoud, F. Réveret, G. Chadeyron, J. Bouaziz, M. Langlet, *Journal of Alloys and Compounds* **2020**, *842*, 155708.
[32] A. Revaux, G. Dantelle, D. Decanini, F. Guillemot, A.-M. Haghiri-Gosnet, C. Weisbuch, J.-P. Boilot, T. Gacoin, H. Benisty, *Nanotechnology* **2011**, *22*, 365701.
[33] V. A. Markel, *J. Opt. Soc. Am. A* **2016**, *33*, 1244.
[34] B. E. A. Saleh, M. C. Teich, *Fundamentals of Photonics, 2nd Edition*, **2007**.
[35] D. G. Hall, in *Progress in Optics*, Elsevier, **1991**, pp. 1–63.